Compact Infrared Hyperspectral Imaging Polarimeter

Julia Craven, Michael W. Kudenov, Maryn G. Stapelbroek, Eustace L. Dereniak

College of Optical Sciences, The University of Arizona
1630 E. University Blvd., Tucson, AZ 85721

ABSTRACT

A compact SWIR/MWIR infrared hyperspectral imaging polarimeter (IHIP) is currently under development at the Optical Detection Lab at the University of Arizona. The sensor uses a pair of sapphire Wollaston prisms and high order retarders to form an imaging birefringent Fourier transform spectropolarimeter. Polarimetric data are acquired through the use of channeled spectropolarimetry to modulate the spectrum with the Stokes parameter information. The two dimensional interferogram is Fourier filtered and reconstructed to recover the complete Stokes vector data across the image. The IHIP operates over a +/-5° field of view and will use a dual-scan false signature reduction technique to suppress polarimetric aliasing artifacts. We present current instrument development progress, initial laboratory results, and our plan for future work.

Keywords: channeled spectropolarimetry, polarimeter, imaging Fourier transform spectrometer, birefringent interferometer, sapphire.

1. INTRODUCTION

Imaging spectrometers are emerging as an important technology in a variety of fields [1]. Dispersive imaging spectrometers, which often utilize a slit with a grating or a prism, are a commonly implemented hyperspectral solution. However, imaging Fourier transform spectrometers offer an alternative technology that can maintain the multiplex (Fellgett) and throughput (Jacquinot) advantages over dispersive systems, resulting in higher signal-to-noise ratios [2]. Additionally, Fourier transform spectrometers (FTS) offer further advantages when implementing channeled spectropolarimetry (CS) [3], thus creating a Fourier transform channeled spectropolarimeter (FTSP) [4]. FTSP is capable of simultaneously measuring the Stokes vector, $\bar{S}$, which is composed of the four Stokes parameters, S_0, S_1, S_2, and S_3. The Stokes parameters are defined by a series of intensity measurements given by

$$\bar{S} = \begin{bmatrix} S_0(\sigma,x,y) \\ S_1(\sigma,x,y) \\ S_2(\sigma,x,y) \\ S_3(\sigma,x,y) \end{bmatrix} = \begin{bmatrix} I_0(\sigma,x,y)+I_{90}(\sigma,x,y) \\ I_0(\sigma,x,y)-I_{90}(\sigma,x,y) \\ I_{45}(\sigma,x,y)-I_{135}(\sigma,x,y) \\ I_R(\sigma,x,y)-I_L(\sigma,x,y) \end{bmatrix}, \tag{1}$$

where S_0 is the total energy of the beam, S_1 denotes preference for 0° over 90° linear polarization, S_2 for linear 45° over 135°, and S_3 for circular right over circular left polarization states. Using a CS-based FTSP enables spectral carrier frequencies containing the Stokes parameter information to be directly measured in the collected interferogram. Thus, the spectropolarimetric data can be extracted from the time domain directly, yielding higher spectral resolution spectropolarimetric data within any finite range of optical path differences over diffraction-based spectrometers.

The FTSP technique was implemented over the middle wavelength infrared (MWIR) by Kudenov et al. by making use of a commercial Michelson interferometer-based Fourier transform spectrometer [5]. Although an FTSP that uses a Michelson interferometer can provide excellent reconstruction results in the laboratory, this type of interferometer has several characteristics that make it impractical for field use as an imaging spectropolarimeter. Most significantly, because the interferogram is created from light propagating along two uncommon paths, vibration can introduce considerable errors into the measurements. Furthermore, sufficient sampling of the interferogram over spectral regions that include the visible to short wave infrared (SWIR) using a Michelson would

require sub-micron mirror movement, demanding the use of a voice coil or other high sensitivity translation mechanism.

In this paper we introduce a field-portable imaging FTSP that takes advantage of a birefringent interferometer, instead of a moving mirror interferometer such as a Michelson, to produce an infrared hyperspectral imaging polarimeter (IHIP) that operates over the SWIR and MWIR spectral regions ($\lambda = 1.5 - 5$ μm). The IHIP is relatively compact (less than 150 mm long, not including the imaging optics), does not require a high resolution translation mechanism, is significantly less sensitive to vibration due to its common path design, and operates over a field of view of +/-5$^\text{o}$.

We begin by presenting the configuration and interference model for the IHIP in section 2. In section 3, we discuss the current progress in characterizing and calibrating the sensor, including a visibility analysis and our spectral calibration technique. Preliminary imaging spectrometer results acquired with the IHIP both in the lab as well as in the field are then presented in section 4. Laboratory transmission spectra results produced with the IHIP are also compared with results obtained with a commercial FTS. Finally, we briefly introduce initial spectropolarimetric data acquired in the laboratory.

2. SENSOR CONFIGURATION

The birefringent interferometer used in the IHIP is based on an imaging FTS design developed and successfully demonstrated in the visible spectral region by Harvey and Fletcher-Holmes [6]. A schematic of the birefringent interferometer used in the IHIP is depicted in Fig. 1. It consists of a pair of Wollaston prisms (W_1 and W_2) with identical apex angles (θ) and fast axes orientations of +/-45$^\text{o}$ relative to the horizontal (x axis). A high order retarder (R_3), with its fast axis oriented at +45$^\text{o}$, is positioned behind the last Wollaston prism (W_2). Lastly, two linear polarizers (P_1 and P_2), oriented with their transmission axes parallel to the x axis (0$^\text{o}$), are included. Polarizer P_1 uniformly polarizes the incident field, which is decomposed by W_1 into two equal-amplitude but orthogonally-polarized constituents. At the interface of the first prism a small angular divergence is produced. These two orthogonally-polarized rays continue to diverge until the interface of W_2, where they are refracted to propagate collinearly. When used together, W_1 and W_2 provide a spatially uniform retardance (to first order) and retarder R_3 provides an additional retardance that enables a single-sided interferogram to be measured. Polarizer P_2 recombines the polarization state and an imaging lens focuses the rays onto the focal plane array (FPA).
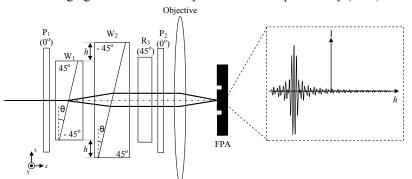

Fig. 1. Imaging Fourier transform spectrometer using a birefringent interferometer. Two Wollaston prisms, W_1 and W_2, and a high order retarder, R_3, are used in series between two polarizers, P_1 and P_2. An objective lens focuses the interference onto the focal plane array. To assemble an interferogram at each pixel, W_2 is translated while frames of data are collected.

A variation in optical path difference (OPD) is produced by translating the centerline of the second Wollaston prism (W_2) relative to the centerline of the first by a distance h, analogous to translating one of the mirrors in a Michelson-based FTS. As the prism is translated, intensity modulations are recorded at each pixel to collect the two dimensional interferogram. The explicit equation for the OPD of the interferometer for the on-axis pixel is given by

$$OPD(\sigma) = 2B(\sigma)h\tan\theta + B(\sigma)d_3,$$

(2)

where $\sigma = \lambda^{-1}$, $B(\sigma) = (n_o(\sigma) - n_e(\sigma))$ is the birefringence of the crystal, and d_3 is the thickness of retarder R_3. Thus the intensity I collected at a single (n, m) pixel will follow

$$I(n,m,h) \propto \int \frac{1}{2} S_0(n,m,\sigma) \cos(2\pi\sigma OPD(h)) d\sigma.$$

(3)

The data collected across the FPA can be considered a three dimensional interferogram data cube, and the spectrum can be recovered at each pixel via a Fourier transformation. Per Eq. 2, the inclusion of retarder R_3 in the interferometer shifts the OPD origin (*i.e.* the location of the centerburst) by an amount equal to Bd_3 away from *OPD* = 0. The result is a phase-correctable, nearly single-sided interferogram, with almost twice the maximum OPD (OPD_{max}) collected by the FTS for the same maximum W_2 translation, h_{max}. The advantage of shifting the interferogram is that the spectral resolution of an FTS, $\Delta\sigma$, is given by [7]

$$\Delta\sigma = 1/OPD_{max}.$$

(4)

Thus by collecting an almost single-sided interferogram with the IHIP, Eq. 4 implies that the spectral resolution will be improved by nearly a factor of two. Phase correction on this interferogram can be performed using the Mertz phase correction technique [2], which uses the symmetric portion of the interferogram, around the centerburst, to calculate low frequency phase errors.

Implementation of the birefringent design into the IHIP is diagrammed in Fig. 2. To produce an FTSP, two additional high order retarders, R_1 and R_2, are placed in series before the first polarizer, with fast axes orientations at 0° and 45° relative to the horizontal, respectively.
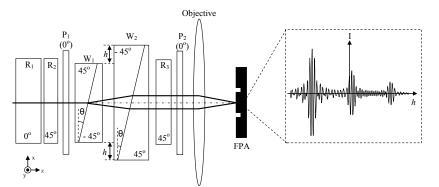

Fig. 2. Schematic of birefringent imaging spectropolarimeter implementation for the IHIP. Two high order retarders, R_1 and R_2, are placed in series before the first polarizer, P_1, of the interferometer. The retarders modulate the interferogram at each pixel with carrier frequencies containing the polarimetric information.

The form of the interferogram produced by the complete IHIP system can be determined from a Mueller calculus analysis, which gives an intensity distribution of [8]

$$I_{0^o}(\sigma,h) \propto \int \frac{(1+\cos(\varphi_h))}{2} [S_0 + S_1 \cos(\varphi_2) + S_2 \sin(\varphi_1)\sin(\varphi_2) - S_3 \cos(\varphi_1)\sin(\varphi_2)] d\sigma.$$

(5)

In Eq. 5, the S_i ($i = 0..3$) are the Stokes parameters. The phase terms corresponding to the OPDs introduced by the spectropolarimetry retarders and the interferometer are given by

$$\phi_1(\sigma) = 2\pi B(\sigma) d_1 \sigma,$$

(6)

$$\phi_2(\sigma) = 2\pi B(\sigma) d_2 \sigma,$$

(7)

$$\phi_h(\sigma) = 2\pi B(\sigma)\sigma(h\tan(\theta) + d_3),$$

(8)

where d_1 and d_2 are the thicknesses of retarders R_1 and R_2, respectively. Expanding Eq. 5 yields seven frequency channels that contain the polarimetric information

$$I(\sigma, h) \propto \int \left\{ \begin{array}{l} \dfrac{S_0}{2}\cos(\varphi_h) + \dfrac{S_1}{4}\left[\cos(\varphi_h + \varphi_2) + \cos(\varphi_h - \varphi_2)\right] + \\[2mm] \dfrac{S_2}{8}\left[\cos(\varphi_h + \varphi_1 + \varphi_2) + \cos(\varphi_h - \varphi_1 - \varphi_2) - \cos(\varphi_h + \varphi_1 - \varphi_2) - \cos(\varphi_h - \varphi_1 + \varphi_2)\right] + \\[2mm] \dfrac{S_3}{8}\left[\sin(\varphi_h + \varphi_1 + \varphi_2) + \sin(\varphi_h - \varphi_1 - \varphi_2) - \sin(\varphi_h + \varphi_1 - \varphi_2) + \sin(\varphi_h - \varphi_1 + \varphi_2)\right] \end{array} \right\} d\sigma. \tag{9}$$

Several of the channels present in Eq. 9 contain duplicate or conjugate information. Consequently, only three distinct channels must be collected to simultaneously measure the complete Stokes vector. The three channels ($C_{0\text{-}2}$) that will be collected for analysis using the IHIP are,

$$C_0 = \int \frac{S_0}{2}\cos\left(\phi_h\right) d\sigma, \tag{10}$$

$$C_1 = \int \frac{S_1}{4}\cos\left(\phi_h - \phi_1\right) d\sigma, \text{ and} \tag{11}$$

$$C_2 = \int \left[-\frac{S_2}{8}\cos\left(\phi_h - \phi_1 + \phi_2\right) + \frac{S_3}{8}\sin\left(\phi_h - \phi_1 + \phi_2\right) \right] d\sigma. \tag{12}$$

Fig. 3 depicts the three channels superimposed on a simulated interferogram for the on-axis pixel, where a 22.5° linear incident polarization state and a spectrally flat, $\lambda = 3 - 5$ µm source was used to produce the interferogram.
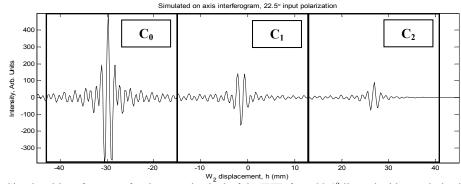

Fig. 3. Simulated interferogram for the on-axis pixel of the IHIP for a 22.5° linear incident polarization state with the polarimetric channels, $C_{0\text{-}2}$, superimposed. Each channel is used to reconstruct one or two of the Stokes parameters.

Filtering these three channels and performing a Fourier transformation allows for the recovery of the Stokes parameters, with S_1, S_2, and S_3 modulated by the carrier frequencies produced by the CS retarders,

$$\Im\left(C_0\right) = \frac{1}{2} S_0\left(\sigma\right), \tag{13}$$

$$\Im\left(C_1\right) = \frac{1}{4} S_1\left(\sigma\right)\exp\left(-j\phi_2\right), \text{ and} \tag{14}$$

$$\Im\left(C_2\right) = \frac{1}{8}\left(-S_2\left(\sigma\right) + jS_3\left(\sigma\right)\right)\exp\left(j\phi_2\right)\exp\left(-j\phi_1\right). \tag{15}$$

In order to characterize the carrier frequency phase factors, φ_1 and φ_2, and thereby demodulate the unknown Stokes parameters, a calibration routine must be implemented. Multiple techniques exist for performing this polarimetric calibration. One such technique, referred to as the 'reference beam calibration technique,' [5] involves measuring a

known reference polarization state to remove the modulating phase factors. More sophisticated calibration methods, such as the 'self calibration technique,' [9] allow for calibration without the need to collect reference data and can provide enhanced calibration accuracy given temperature variations. In addition, while crystal dichroism features present in the CS retarders can produce spectropolarimetric reconstruction errors if not accounted for [5], a 3:1 CS retarder thickness ratio (d_1:d_2) is used in the IHIP, ensuring that any dichroism artifacts will be produced in channels not collected or used by the IHIP for spectropolarimetric reconstructions.

The layout of the IHIP also makes the instrument ideal for implementation of the 'false signature reduction technique' (FSRT) [10], which can be used to reduce aliasing artifacts in CS reconstructions produced by the presence of S_0 information in the CS channels, as well as to improve the spectral resolution of S_0 reconstructions by up to a factor of four. FSRT can be implemented with the IHIP by collecting two sets of data. The first set will use the optical layout depicted in Fig. 2, and the interferogram collected at a single pixel will be of the form of Eq. 5. By rotating both polarizers, P_1 and P_2 of Fig. 2, by 90 degrees from the horizontal before collecting a second interferogram, the functional form of this second data set for a single pixel will now follow [8]

$$I_{0^\circ}(\sigma,h) \propto \int \frac{(1+\cos(\varphi_h))}{2} \big[S_0 - S_1 \cos(\varphi_2) - S_2 \sin(\varphi_1)\sin(\varphi_2) + S_3 \cos(\varphi_1)\sin(\varphi_2)\big] d\sigma. \tag{16}$$

Eq. 16 demonstrates an 180° phase change in the carrier frequencies modulating S_1, S_2, and S_3 onto the collected interferogram, relative to Eq. 5. Thus by appropriately weighting and summing the two interferograms, an interferogram containing only the S_0 Stokes parameter can be extracted. This high spectral resolution S_0 data can be subtracted from the CS channels C_1 and C_2 prior to the reconstruction of S_1, S_2, and S_3, thereby improving the quality of the measured Stokes parameters.

The assembly and calibration of the IHIP is in progress. A photograph of the sensor in its current configuration is provided in Fig. 4 (a), while a 3D wire grid schematic of the sensor is presented in Fig. 4 (b). The CS retarders (R_1 and R_2) have not been added to the system, and thus the sensor operates as an imaging FTS. Holographic wire grid polarizers on a CaF_2 substrate are used for polarizers P_1 and P_2. All birefringent elements are sapphire and are anti-reflection (AR) coated for $\lambda = 1.5 - 5$ μm. The dimensions of the Wollaston prisms are 44x44x11.75 mm for W_1, and 44x135x27.8 mm for W_2, with a fabrication tolerance of +/- 0.1 mm on each dimension. The apex angle of all four prism wedges is nominally 10 degrees with a +/- 0.1 degree tolerance. Retarders R_1, R_2, and R_3 are cylindrical 50 mm diameter elements, with thicknesses of 30 mm, 10 mm, and 10.5 mm, respectively. A commercial translation stage (Physik Intrumente 404PD) is used to translate W_2 for a total displacement of 100 mm. A rotary encoder used in combination with a rack and pinion gear system monitors the stage movement in 10 μm increments. The signal produced by the encoder is electronically interfaced with a Technological Arts HSC12 microcontroller which then triggers the camera to collect a frame of data for a stage displacement of Δh. To sample the interferogram without aliasing across the $\lambda = 1.5 - 5$ μm spectral band with the IHIP, the camera must take a frame of data every $\Delta h \le 273$ μm ; for the data presented here, we selected $\Delta h = 200$ μm .

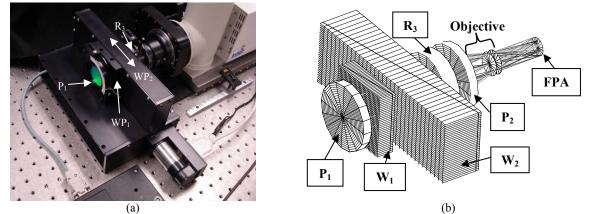

(a)   (b)

Fig. 4. (a) Photograph of the sensor in its current configuration. Retarders R_1 and R_2 have not been added to the system and thus the instrument operates as an imaging Fourier transform spectrometer. (b) Zemax wire grid model of the birefringent interferometer and imaging optics.

For the data presented in this paper, the IHIP is used with a 320x256 element indium antimonide (InSb) Indigo Merlin lab camera (3 – 5 μm). However, the imaging optics and camera for the final system will incorporate a closed-cycle InSb camera (for field portability) optimized for a spectral passband spanning 1.5 – 5 μm.

3. VISIBILITY ANALYSIS AND SPECTRAL CALIBRATION

Once the imaging FTS portion of the IHIP was assembled, the first tasks performed included a fringe visibility analysis to assess signal-to-noise performance and a spectral calibration of the birefringent interferometer.

3.1 Fringe Visibility Calculation

One important metric in characterizing interference is fringe visibility, which is a contrast ratio relating the maximum and minimum intensities, defined as

$$V = \frac{I_{max} - I_{min}}{I_{max} + I_{min}}, \tag{17}$$

where V is the visibility (ranging from 0 to 1) and I_{max}, I_{min} are the maximum and minimum intensities in the local fringe field, respectively. Highly visible fringes are desired to yield the best possible signal-to-noise ratios for IHIP spectral reconstructions. In an interferometer such as the IHIP, fringe visibility will decrease when the rays are not properly localized at the detector plane. Thus visibility can decrease if the two coherent point spread functions (PSFs) are only interfering on their peripheries, as opposed to being directly coincident with one another [11]. While ray tracing simulations indicate that some loss of fringe visibility across the field of view is inherent to the birefringent interferometer design used for the IHIP, this decrease of fringe visibility can be exacerbated by deviations from ideal specifications in the fabricated birefringent elements, such as variations in the apex angles of the Wollaston prisms.

To quantify the fringe visibility across the field of a view, interferograms of a HeNe laser spot (λ = 3.39 μm) from a Jodon 5 mW laser are acquired using the birefringent interferometer with the Indigo camera in the experimental setup depicted in Fig. 5. The laser spot is imaged in reflection off of a clay brick. Nine different data sets are collected with the spot moved using a planar mirror in a kinematic mount to nine different positions in an approximate 3-by-3 grid spanning the field of view.
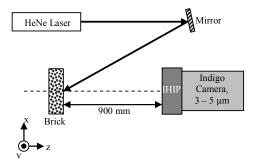

Fig. 5. Experimental setup for visibility analysis. A HeNe laser (λ = 3.39 μm) spot is imaged after reflecting off of a brick using the birefringent interferometer and the Indigo Camera.

An interferogram collected at a single pixel during these visibility tests as W$_2$ is translated 100 mm is presented in Fig. 6 (a), where the detector offset has been removed. The modulations in the interferogram remain at relatively constant amplitude for the complete data collection. Using Eq. 17, we find the visibility for this data set is $V = 0.92$. Repeating this procedure for the 8 other spot locations across the field of view yields the visibility map depicted in Fig. 6 (b). These results indicate that the fringe visibility at λ = 3.39 μm can be expected to range from approximately 0.86 to 0.96 across the image plane. In general, visibility values of $V \geq 0.2$ are detectable [12], and the values measured indicate highly visible fringes. Due to the changing size of the Airy disk across the SWIR and

MWIR, PSF overlap will vary across the spectral bandpass. Thus visibility values are expected to be slightly lower or slightly higher for wavelengths smaller than or larger than that of the HeNe used for this study, respectively.
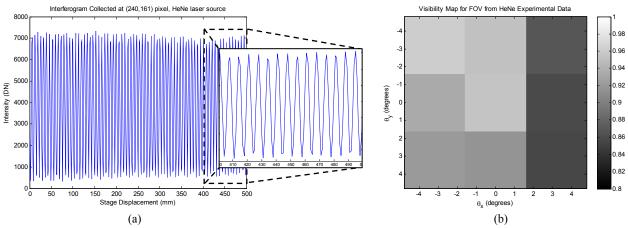

Fig. 6. Results from the visibility tests with the HeNe laser. (a) Interferogram of the HeNe laser spot, collected at the (x,y) = (240,161) pixel on the InSb array. (b) Approximate visibility map based on 9 interferograms collected across the field of view of the IHIP.

3.2 Spectral Calibration

Spectral calibration of the birefringent interferometer involves compensating for the dispersion of the birefringent sapphire material, used for the Wollaston prisms and retarders, over the $\lambda = 1.5 - 5$ μm spectral band. As evident from Eq. 2 for our system, the optical path difference will vary as a function of wavelength if the birefringent material exhibits dispersion. This results in a spectrally varying Nyquist frequency, f_{ny}, where

$$f_{ny}(\sigma) = \frac{1}{2\Delta OPD} = \frac{1}{4B(\sigma)\tan(\alpha)\Delta h}.$$ (18)

In Eq. 18, ΔOPD is the change in OPD between frames of data, corresponding to a displacement of the translation stage Δh, where $\Delta h \leq 273$ μm in order to sample the interferogram without aliasing. Without compensation for this dispersion effect, the spectral reconstructions recovered will not be representative of the actual spectra measured.

Dispersion compensation can be performed by first using the Sellmeier equation with the appropriate coefficients for both the extraordinary (n_e) and the ordinary (n_o) indices of sapphire [13] to model the birefringence as a function of wavenumber (cm^{-1}) over the band of interest. As depicted in Fig. 7 (a), the Sellmeier equation indicates that the birefringence of sapphire exhibits a rapid increase at lower wavenumbers ($B = 0.005645 - 0.007594$ for $\sigma = 2000$ cm^{-1} – 3500 cm^{-1}, respectively), followed by a slower increase for the remainder of the spectral band, to a maximum value of 0.007805 at 6667 cm^{-1}.

Once a model for the dispersion of the birefringence is acquired, a relative birefringence, γ, is calculated by normalizing the birefringence to the value at a single wavelength,

$$\gamma = \frac{B(\sigma)}{B(\sigma_{ref})}.$$ (19)

For spectral calibration of the IHIP, we arbitrarily select $\sigma_{ref} = 6667$ cm^{-1}. Once γ has been calculated, the uncompensated spectral axis for the IHIP reconstructions, $\bar{\sigma}$, found by calculating $f_{ny}(\sigma_{ref})$, is weighted by γ to correct for the dispersion errors

$$\bar{\sigma}' = \gamma\bar{\sigma},$$ (20)

where $\bar{\sigma}'$ is the dispersion compensated spectral axis. The final step in spectral calibration involves interpolating the reconstructed spectral data to the corrected spectral axis. This is accomplished for the IHIP by using a built in interpolation function in MatLab. Spectral calibration can be performed using this technique at every pixel across the FPA.
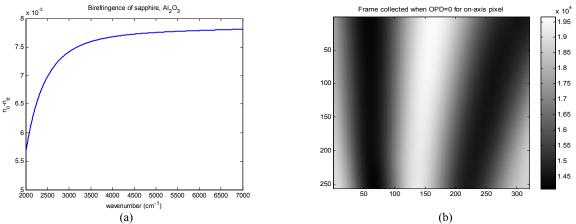

Fig. 7. (a) The dispersion of the birefringence of sapphire. (b) A frame of data captured with the IHIP. The centerburst is captured for the on-axis pixel, but a fringe field is present across the FPA.

An additional consideration during spectral calibration is the spatial variation of the centerburst's OPD offset as a function of field angle. Fig. 7 (b) illustrates this effect by depicting a frame of data collected with the IHIP when imaging a uniform temperature hot plate. Here, the centerburst is captured for the on-axis $(0^\circ, 0^\circ)$ pixel, but a hyperbolic fringe pattern [6] is collected across the image, indicating that the location of the centerburst spans a range of translation stage positions (h). This deviation in the centerburst position for the three dimensional interferogram results in a variation in the spectral resolution of the IHIP across the field of view, as the spectral resolution is inversely proportional to the maximum OPD, $\Delta\sigma = 1/OPD_{max}$ [7]. While the change in spectral resolution is small ($\Delta\sigma = 44.5 - 46.3$ cm^{-1}), the effect produces a different spectral axis ($\bar{\sigma}$) at each (n,m) pixel, and thus a different dispersion compensated spectral axis, $\bar{\sigma}'$, is required at each pixel location.

Once dispersion compensation has been performed, the calibration is tested in the laboratory using two different sources. First, the $\sigma = 2950$ cm^{-1} ($\lambda = 3.39$ μm) HeNe laser spot is imaged approximately on-axis using the setup depicted in Fig. 5. Additionally, the uniform temperature hotplate at 106°C was used to collect a second set of data while being imaged approximately 600 mm from the IHIP. Fig. 8 (a) and (b) display the spectral reconstructions for the laser and the hotplate, respectively. Reconstructions both with and without dispersion compensation are depicted. Fig. 8 (a) demonstrates a shift in the peak of the sharp laser line from $\sigma = 2867$ cm^{-1} for the uncompensated data to $\sigma = 2952$ cm^{-1} after dispersion compensation. The hotplate data depicted in Fig. 8 (b) shows significant error without dispersion compensation; the 2000 - 3100 cm^{-1} spectral bandpass of the imaging optics, as well as the CO_2 absorption line at $\sigma = 2336$ cm^{-1} ($\lambda = 4.28$ μm), are skewed to lower wavenumber values. However with dispersion compensation, the bandpass of the lens is correctly presented and the CO_2 absorption line is found at $\sigma = 2331$ cm^{-1}.
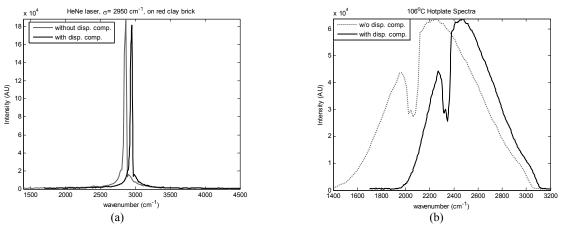
Fig. 8. Reconstructed spectra with and without dispersion compensation. (a) A HeNe laser source, (b) a uniform temperature hot plate. Without dispersion compensation, the spectra are not accurately presented. However, with dispersion compensation, the spectral reconstructions accurately reflect the input spectra.

4. RESULTS

With spectral calibration complete, the IHIP was first used to reconstruct transmission spectra in the laboratory. The experimental setup is depicted in Fig. 9 (a). A variable temperature hot plate set at a uniform temperature of 106° C is used as a source and fills the field of view of the sensor. The scene used in front of the hotplate, as imaged by the Indigo camera, is depicted in Fig. 9 (b), where the detector's radiometric offset has been removed. The three objects which compose the scene are, as labeled, an overhead transparency, a compact disc jewel case cover, and two layers of a plastic garbage bag taped to an optical mount.
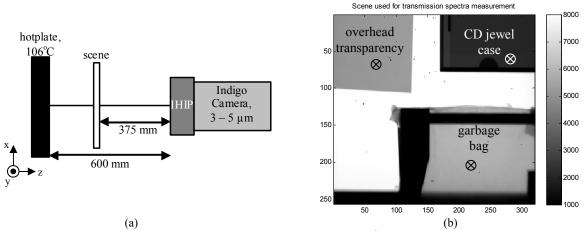

Fig. 9. Transmission spectra experiment. (a) Experimental setup. A 106 °C hotplate is used as a source behind a scene of various plastic targets. (b) The scene, as imaged by the Indigo camera. Each object is labeled.

For all data sets, data were averaged after phase correction over 10 consecutive interferograms. Transmission spectra are calculated from interferograms collected at three different arbitrarily selected pixels across the image, whose approximate locations are marked by three '$\otimes$' in Fig. 9 (b). Data were also collected for the hotplate with the scene removed as reference spectra. The transmission spectrum at each (n,m) pixel, $T_{n,m}(\sigma)$, was calculated using

$$T_{n,m}(\sigma) = \frac{S_0^{plastic}(\sigma,n,m)}{S_0^{hotplate}(\sigma,n,m)}, \tag{21}$$

where $S_0^{plastic}(\sigma,n,m)$ and $S_0^{hotplate}(\sigma,n,m)$ are the phase-corrected averaged spectra reconstructed from the interferograms collected by the Indigo camera at the (n, m) pixel with the scene in front of the hotplate and with the

scene removed, respectively. In calculating the spectra used in Eq. 21, we assumed a linear detector response, where the output digital number counts (*DN*) can be modeled by the equation [14]

$$DN(n,m,\phi) = R(n,m)\phi + O(n,m),$$ (22)

where R is the pixel responsivity, φ is the photon flux, and O is the pixel offset.

The reconstructed spectra for the three pixels are depicted in Fig. 10 (a). The spectral resolution for these reconstructions is $\Delta\sigma \approx 45.4$ cm^{-1}. For comparison, spectra for the three plastic objects used in the scene were acquired using a commercial Oriel MIR8000 infrared FTS with an 80026 MCT detector and an 80007 Silicon Carbide source. The transmission spectra obtained using Eq. 21 with the Oriel FTS, at an equivalent spectral resolution to that of the IHIP, are depicted in Fig. 10 (b). Comparing the two sets of transmission spectra indicates that the data recovered from both spectrometers is in good correspondence, indicating that the spectrally calibrated IHIP can accurately recover spectral data. Variations in percent transmissions between the two sets of data are attributed to nonlinear detector effects, as well as emissions from, and variations in temperatures of, the plastic objects.
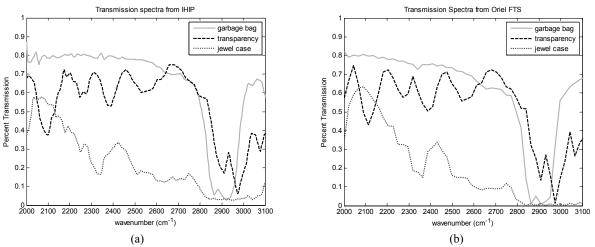

Fig. 10. (a) Transmission spectra for the three pixel locations marked in Fig. 9b, as reconstructed by the IHIP. (b) Transmission spectra for the objects from a commercial FTS.

Next, the IHIP was used to collect spectral data outdoors. The system was relocated to a parking lot on the University of Arizona campus and was used to collect an interferogram of the scene depicted in Fig. 11 (a), as imaged by the Indigo camera. As shown, the scene was composed of several parked cars and vegetation behind a running pickup truck with its lights on. The interferogram of the truck engine, collected at the $(x, y) = (122,157)$ pixel, is also presented in Fig. 11 (a), with the corresponding pixel location indicated by the dashed arrow. The spectrum recovered from this interferogram is depicted in Fig. 11 (b). Although the spectrum is relatively noisy, the sharp CO_2 absorption feature at 2338 cm^{-1} is clearly present. We attribute the high amount of noise in the outdoor reconstruction to the slow scan time that must be implemented for W_2 with the Indigo camera, which is limited to data collection at 7.5 frames per second, as well as the low DN count in the scene relative to the detector offset. It is anticipated that data quality will improve with the implementation of a higher frame rate (at least 125 Hz), closed cycle camera that operates over the entire $\lambda = 1.5 - 5$ μm spectral band, which will be used for data collection in the future.
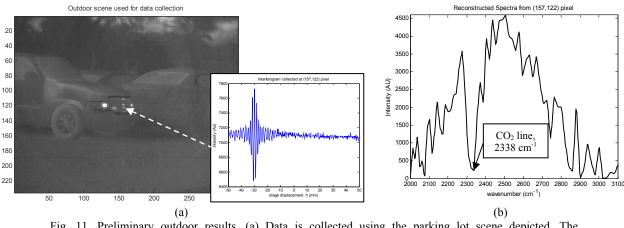
Fig. 11. Preliminary outdoor results. (a) Data is collected using the parking lot scene depicted. The interferogram of a single pixel, from the engine, is also presented. (b) Spectrum recovered from this single pixel clearly demonstrates the CO_2 absorption line.

Finally, to demonstrate the spectropolarimetric properties of the system, the CS retarders, R_1 and R_2, are added to the IHIP in the laboratory. A photograph of the complete IHIP system is provided in Fig. 12 (a). For the collection of initial channeled interferogram data, the hotplate is used as a uniform 73° C source behind a CaF_2 wire grid polarizer oriented at approximately 22.5^o relative to the horizontal. The polarizer is imaged by the IHIP and the Indigo camera, and the two dimensional interferogram is assembled.
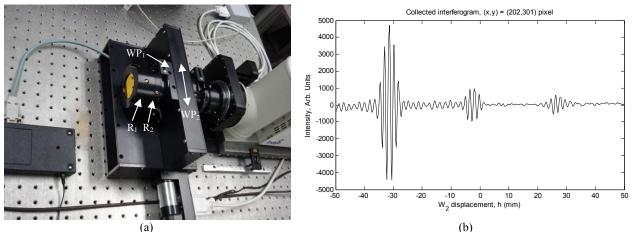

Fig. 12. Preliminary spectropolarimetric data collection. (a) The IHIP setup in the laboratory with the CS retarders mounted to the front of the birefringent interferometer. (b) When imaging a linear polarizer, the interferogram collected at a single pixel contains the CS channels containing the polarization information.

The interferogram from an arbitrarily selected pixel, $(x, y) = (202,301)$, is depicted in Fig. 12 (b). Data were averaged over 10 consecutive interferograms, and a low pass filter has been used to reduce noise. The collected interferogram clearly exhibits the two additional CS channels, aside from the centerburst, that are present in the simulated IHIP interferogram depicted in Fig. 3, and are absent from FTS interferograms measuring purely spectral (S_0) data. Once the IHIP is polarimetrically calibrated, the channeled interferograms collected across the FPA can be reconstructed to produce two dimensional spectropolarimetric data across the SWIR and MWIR.

5. CONCLUSION

In this paper we present our current progress on the development of an infrared hyperspectral imaging polarimeter (IHIP) that will collect two dimensional spectropolarimetric information over the SWIR and MWIR spectral ranges for $\lambda = 1.5 - 5$ μm. The system is a compact, common-path Fourier transform spectropolarimeter that operates over

a +/-5 degree field of view, and can be integrated with commercial camera systems to offer a portable solution for the detection of spectropolarimetric signatures in the field.

The birefringent interferometer used in the IHIP has been assembled, and a fringe visibility analysis and the spectral calibration of the interferometer have been performed. The spectral calibration included compensation for the dispersion of sapphire, the birefringent crystal material, over the spectral band of interest. Once calibrated, laboratory results indicated excellent correspondence in spectral transmission reconstructions relative to a commercial Fourier transform spectrometer. Preliminary outdoor data also demonstrates that the sensor is capable of detecting spectral features in the field, such as the CO_2 absorption line at $\lambda = 4.28$ µm. Finally, the channeled spectropolarimetry retarders were added to the sensor, and initial collected data provided clear illustration of a channeled interferogram, which can be used to reconstruct the Stokes parameters.

Future work on this project will include polarimetric calibration of the complete IHIP sensor, as well as the collection and reconstruction of further spectropolarimetric data. In addition, a closed-cycle camera capable of imaging and detecting the entire $1.5 - 5$ µm bandpass will be integrated in lieu of the Indigo laboratory camera. Once IHIP assembly and calibration is complete, the sensor will be tested through the examination of spectropolarimetric data in the lab and in the field. Furthermore, the false signature reduction technique will be implemented and tested.

ACKNOWLEDGEMENTS

REFERENCES

1. Wolfe, W. L. *Introduction to Imaging Spectrometers*. SPIE Press, Bellingham, WA (1997).
2. Griffiths, P. and Haseth, J.D., *Fourier Transform Infrared Spectrometry*, John Wiley & Sons, Inc., New York, (1986).
3. Oka, K., and Kato, T., "Spectroscopic Polarimetry with a Channeled Spectrum," Opt. Lett. 24, 1475-1477 (1999).
4. Kusunoki, T., and Oka, K., "Fourier spectroscopic measurement of polarization using birefringent retarders," Jap. Soc. of Ap. Phys. 61, 871 (2000).
5. Kudenov, M., Hagen, N., Dereniak, E., et al, "Fourier transform channeled spectropolarimetry in the MWIR," Opt. Exp., 15(20) 12792 – 12805 (2007)
6. Harvey, A.R. and D.W. Fletcher-Holmes, "Birefringent Fourier-transform imaging spectrometer," Opt Express 12 (22), 5368 – 5374 (2004).
7. Saptari, V. *Fourier Transform Spectroscopy Instrumentation Engineering*. SPIE Press, Bellingham, WA (2004).
8. Goldstein, D. *Polarized Light*, Marcel Dekker, New York, (2003).
9. Taniguchi, A., Oka, K., Okabe, H., and Hayakawa, M, "Stabilization of a channeled spectropolarimeter by self-calibration," Opt. Lett. 31, 3279-3281 (2006).
10. Craven, J., Kudenov, M., and Dereniak, E. "False signature reduction in infrared channeled spectropolarimetry," Proc. SPIE, Vol. 7419 (2009).
11. Mahajan, V.N. *Optical Imaging and Aberrations, Pt II*. SPIE Press, Bellingham, WA (2001).
12. Goodwin, E.P., and Wyant, J.C. *Field Guide to Interferometric Optical Testing*, SPIE Press, Bellingham, WA, 2006.
13. *The Infrared Handbook*, Rev. Ed., W. L. Wolfe and G.J. Zissis, Eds., IRIA Center, Michigan (1993).
14. Venkateswarlu, R. M. H. Er, Y. H. Gan, and Y. C. Fong. "Nonuniformity compensation for IR focal plane array sensors," Proc. of SPIE Vol. 3061. pg. 915-926 (1997).